Pramana – J. Phys. (2016) 87: 13
DOI 10.1007/s12043-016-1204-z

Similarities between 2D and 3D convection for large Prandtl number

AMBRISH PANDEY*, MAHENDRA K VERMA, ANANDO G CHATTERJEE and BIPLAB DUTTA

Department of Physics, Indian Institute of Technology, Kanpur 208 016, India
*Corresponding author. E-mail: ambrishiitk@gmail.com

MS received 4 October 2014; revised 28 July 2015; accepted 7 September 2015; published online 18 June 2016

Abstract. Using direct numerical simulations of Rayleigh–Bénard convection (RBC), we perform a comparative study of the spectra and fluxes of energy and entropy, and the scaling of large-scale quantities for large and infinite Prandtl numbers in two (2D) and three (3D) dimensions. We observe close similarities between the 2D and 3D RBC, in particular, the kinetic energy spectrum $E_u(k) \sim k^{-13/3}$, and the entropy spectrum exhibits a dual branch with a dominant k^{-2} spectrum. We showed that the dominant Fourier modes in 2D and 3D flows are very close. Consequently, the 3D RBC is quasi-two-dimensional, which is the reason for the similarities between the 2D and 3D RBC for large and infinite Prandtl numbers.

Keywords. Turbulent convective heat transfer; buoyancy-driven flows; convection.

PACS Nos 47.27.te; 47.55.P–

1. Introduction

Thermal convection is an important mode of heat transport in the interiors of stars and planets, as well as in many engineering applications. Rayleigh–Bénard convection (RBC) is an idealized model of thermal convection, in which a fluid, placed horizontally between two thermally conducting plates, is heated from the bottom and cooled from the top [1]. The resulting convective motion is primarily governed by two nondimensional parameters, the Rayleigh number Ra, which is the ratio between the buoyancy and viscous force, and the Prandtl number Pr, which is the ratio between the kinematic viscosity and thermal diffusivity.

The earth's mantle and viscous fluids have large Prandtl numbers, and their convective flow is dominated by sharp 'plumes'. Schmalzl *et al* [2,3] and van der Poel *et al* [4] showed that for large Prandtl numbers, the flow structures and global quantities, e.g., the Nusselt number and Reynolds number, exhibit similar behaviour for three dimensions (3D) and two dimensions (2D). In the present paper, we analyse the flow behaviour of 2D and 3D flows for large Prandtl numbers, and show that the flow in the third direction in 3D RBC gets suppressed, and the large-scale Fourier modes of 2D and 3D RBC are very similar.

The energy and entropy spectra are important quantities in Rayleigh–Bénard convection, and have been studied extensively for various Prandtl numbers [5–13]. Pandey *et al* [13], in their numerical simulations for very large Prandtl numbers in three dimensions, reported that the kinetic energy spectrum $E_u(k)$ scales as $k^{-13/3}$, and the entropy spectrum $E_\theta(k)$ shows a dual branch with a dominant k^{-2} spectrum. They also showed that the scaling of the energy and entropy spectra are similar for the free-slip and no-slip boundary conditions, apart from the prefactors.

In this study, we performed 2D and 3D RBC simulations for the Prandtl numbers 10^2, 10^3, and ∞, and the Rayleigh numbers between 10^5 and 5×10^8. We compute the ten most dominant Fourier modes of 2D and 3D flows, and show them to be very close, which is the reason for the similarities between 2D and 3D RBC. We compute the spectra and fluxes of energy and entropy for 2D and 3D flows, and show them to be very similar. We also show that the viscous and thermal dissipation rates for 2D and 3D RBC behave similarly. For completeness and validation, we demonstrate similarities between the Nusselt and Péclet numbers and temperature fluctuations for 2D and 3D RBC, consistent with the earlier results of Schmalzl *et al* [2,3], van der Poel *et al* [4], and Silano *et al* [14].

The paper is organized as follows: In §2, we discuss the governing equations for large and infinite Prandtl numbers. Details of our numerical simulations are provided in §3. In §4, we compare the most dominant Fourier modes of 2D and 3D RBC for $\mathrm{Pr} = \infty$. In §5, we discuss the spectra and fluxes of the kinetic energy and entropy. Scaling of large-scale quantities such as the Nusselt and Péclet numbers, the temperature fluctuations, and the viscous and thermal dissipation rates are discussed in §6. We conclude in §7.

2. Governing equations

The equations of Rayleigh–Bénard convection under Boussinesq approximation for a fluid confined between two plates separated by a distance d are

$$\frac{\partial \mathbf{u}}{\partial t} + (\mathbf{u}\cdot\nabla)\mathbf{u} = -\nabla\sigma + \theta\hat{z} + \sqrt{\frac{\mathrm{Pr}}{\mathrm{Ra}}}\nabla^2\mathbf{u}, \tag{1}$$

$$\frac{\partial \theta}{\partial t} + (\mathbf{u}\cdot\nabla)\theta = u_z + \frac{1}{\sqrt{\mathrm{PrRa}}}\nabla^2\theta, \tag{2}$$

$$\nabla\cdot\mathbf{u} = 0, \tag{3}$$

where $\mathbf{u} = (u_x, u_y, u_z)$ is the velocity field, θ and σ are the deviations of the temperature and pressure fields from the conduction state, and $\hat{z}$ is the buoyancy direction. The two nondimensional parameters are Rayleigh number $\mathrm{Ra} = \alpha g \Delta d^3/\nu\kappa$ and the Prandtl number $\mathrm{Pr} = \nu/\kappa$, where Δ is the temperature difference between the top and bottom plates, g is the acceleration due to gravity, and α, ν, and κ are the heat expansion coefficient, kinematic viscosity, and thermal diffusivity of the fluid, respectively. The above nondimensional equations are obtained by using d, $\sqrt{\alpha g \Delta d}$, and Δ as the length, velocity, and temperature scales, respectively.

For very large Prandtl numbers, $\sqrt{\alpha g \Delta d/\mathrm{Pr}}$ is used as the velocity scale for the nondimensionalization, which yields

$$\frac{1}{\mathrm{Pr}}\left[\frac{\partial \mathbf{u}}{\partial t} + (\mathbf{u}\cdot\nabla)\mathbf{u}\right] = -\nabla\sigma + \theta\hat{z} + \frac{1}{\sqrt{\mathrm{Ra}}}\nabla^2\mathbf{u}, \tag{4}$$

$$\frac{\partial \theta}{\partial t} + (\mathbf{u}\cdot\nabla)\theta = u_z + \frac{1}{\sqrt{\mathrm{Ra}}}\nabla^2\theta, \tag{5}$$

$$\nabla\cdot\mathbf{u} = 0. \tag{6}$$

In the limit of infinite Prandtl number, eq. (4) reduces to a linear equation [13]

$$-\nabla\sigma + \theta\hat{z} + \frac{1}{\sqrt{\mathrm{Ra}}}\nabla^2\mathbf{u} = 0. \tag{7}$$

In the Fourier space, the above equation transforms to

$$-i\mathbf{k}\hat{\sigma}(\mathbf{k}) + \hat{\theta}(\mathbf{k})\hat{z} - \frac{1}{\sqrt{\mathrm{Ra}}}k^2\hat{\mathbf{u}}(\mathbf{k}) = 0, \tag{8}$$

where $\hat{\sigma}$, $\hat{\theta}$, and $\hat{\mathbf{u}}$ are the Fourier transforms of σ, θ, and $\mathbf{u}$, respectively, and $\mathbf{k} = (k_x, k_y, k_z)$ is the wave vector. Using the constraint that the flow is divergence-free, i.e., $\mathbf{k}\cdot\hat{\mathbf{u}}(\mathbf{k}) = 0$, the velocity and pressure fields can be expressed in terms of temperature fluctuations as [13]

$$\hat{\sigma}(\mathbf{k}) = -i\frac{k_z}{k^2}\hat{\theta}(\mathbf{k}), \tag{9}$$

$$\hat{u}_z(\mathbf{k}) = \sqrt{\mathrm{Ra}}\frac{k_\perp^2}{k^4}\hat{\theta}(\mathbf{k}), \tag{10}$$

$$\hat{u}_{x,y}(\mathbf{k}) = -\sqrt{\mathrm{Ra}}\frac{k_z k_{x,y}}{k^4}\hat{\theta}(\mathbf{k}), \tag{11}$$

where $k_\perp^2 = k_x^2 + k_y^2$ in 3D and $k_\perp^2 = k_x^2$ in 2D (assuming $k_y = 0$). Using these relations, the kinetic energy E_u can be expressed in terms of entropy as

$$E_u(\mathbf{k}) = \frac{1}{2}|\hat{\mathbf{u}}(\mathbf{k})|^2 = \frac{1}{2}\mathrm{Ra}\frac{k_\perp^2}{k^6}|\hat{\theta}(\mathbf{k})|^2 = \mathrm{Ra}\frac{k_\perp^2}{k^6}E_\theta(\mathbf{k}). \tag{12}$$

For the $\mathrm{Pr} = \infty$ limit, the nonlinear term for the velocity field, $(\mathbf{u}\cdot\nabla)\mathbf{u}$, is absent, and the pressure, buoyancy, and viscous terms are comparable to each other. Assuming that the large-scale Fourier modes dominate the flow, we can estimate the ratios of these terms by computing them for the most dominant $\mathbf{u}(\mathbf{k})$ that occurs for $\mathbf{k} = (\pi/\sqrt{2}, 0, \pi)$. Hence, the aforementioned ratios can be estimated to be approximately

$$\frac{|\theta|}{|\nabla\sigma|} \approx \frac{|\theta(\mathbf{k})|}{|k\sigma(\mathbf{k})|} \approx \frac{k}{k_z} \approx 1, \tag{13}$$

$$\frac{|\theta|}{|\nabla^2\mathbf{u}|/\sqrt{\mathrm{Ra}}} \approx \frac{|\theta(\mathbf{k})|}{|k^2\mathbf{u}(\mathbf{k})/\sqrt{\mathrm{Ra}}|} \approx \frac{k}{k_\perp} \approx 1. \tag{14}$$

For very large Pr, the nonlinear term for the velocity field, $(\mathbf{u}\cdot\nabla)\mathbf{u}$, is weak, and consequently the kinetic energy flux is very weak in this regime. The flow is dominated by the pressure, buoyancy, and viscous terms similar to that for the $\mathrm{Pr} = \infty$ limit. The nonlinearity of the temperature equation, $(\mathbf{u}\cdot\nabla)\theta$, however is quite strong, and it yields a finite entropy flux for large and infinite Prandtl numbers. We shall demonstrate this statement using numerical data.

In this paper, we solve RBC for large and infinite Pr; for large Pr, we solve eqs (4)–(6), while for $\mathrm{Pr} = \infty$, we solve eqs (7), (5), (6). In the next section, we describe the numerical method used for our simulations.

3. Numerical method

We solve the governing equations [eqs (4)−(6)] for large Prandtl numbers and eqs (7), (5), (6) for $\mathrm{Pr} = \infty$. The box geometry of the 2D simulations is $2\sqrt{2} : 1$, and that for the 3D simulations is $2\sqrt{2} : 2\sqrt{2} : 1$. For the horizontal plates, we employ stress-free boundary condition for the velocity field, and conducting boundary condition for the temperature field. However, for the vertical side walls, periodic boundary condition is used for both the temperature and velocity fields. The fourth-order Runge–Kutta method is used for the time

Table 1. Details of our free-slip numerical simulations: N_x, N_y and N_z are the number of grid points in x-, y-, and z-directions, respectively. The computed viscous dissipation rates $C_{\epsilon_u}^{\mathrm{comp.}}$ are in good agreement with the corresponding estimated values $C_{\epsilon_u}^{\mathrm{est.}}$ $[=(\mathrm{Nu}-1)\mathrm{Ra}/\mathrm{Pe}^2]$. Similarly, the computed thermal dissipation rates $C_{\epsilon_T,1}^{\mathrm{comp.}}$ and $C_{\epsilon_T,2}^{\mathrm{comp.}}$ agree with the corresponding estimated values $C_{\epsilon_T,1}^{\mathrm{est.}}$ [=Nu] and $C_{\epsilon_T,2}^{\mathrm{est.}}$ $[=(\mathrm{Nu}/\mathrm{Pe})(\Delta/\theta_L)^2]$ reasonably well. For all the simulations $k_{\max}\eta_\theta \geqslant 1$, indicating that our simulations are well resolved.

Pr	Ra	$N_x \times N_y \times N_z$	Nu	Pe	$C_{\epsilon_u}^{\mathrm{comp.}}$	$C_{\epsilon_u}^{\mathrm{est.}}$	$C_{\epsilon_T,1}^{\mathrm{comp.}}$	$C_{\epsilon_T,2}^{\mathrm{comp.}}$	$C_{\epsilon_T,2}^{\mathrm{est.}}$	$k_{\max}\eta_\theta$
10^2	1×10^5	$256 \times 1 \times 128$	9.8	1.98×10^2	22.3	22.3	9.8	0.61	0.61	2.9
10^2	5×10^5	$256 \times 1 \times 128$	14.5	4.98×10^2	28.5	27.3	14.5	0.37	0.35	1.8
10^2	1×10^6	$512 \times 1 \times 128$	17.3	7.16×10^2	34.4	31.8	17.3	0.31	0.29	2.0
10^2	5×10^6	$512 \times 1 \times 256$	27.4	1.84×10^3	42.5	38.9	27.4	0.19	0.18	1.7
10^2	1×10^7	$1024 \times 1 \times 256$	34.7	3.13×10^3	36.5	34.5	34.7	0.14	0.13	1.9
10^2	5×10^7	$1024 \times 1 \times 512$	61.6	1.03×10^4	28.7	28.6	61.6	0.072	0.072	1.5
10^2	1×10^8	$2048 \times 1 \times 512$	79.8	1.70×10^4	27.1	27.1	79.8	0.056	0.056	1.7
10^3	1×10^5	$256 \times 1 \times 128$	9.8	1.98×10^2	22.3	22.3	9.8	0.60	0.60	1.6
10^3	5×10^5	$512 \times 1 \times 128$	16.0	5.36×10^2	26.1	26.1	16.0	0.36	0.36	1.4
10^3	1×10^6	$512 \times 1 \times 256$	19.8	8.24×10^2	27.7	27.7	19.8	0.29	0.29	1.5
10^3	5×10^6	$1024 \times 1 \times 512$	28.9	2.10×10^3	33.2	31.7	28.9	0.17	0.16	1.9
10^3	1×10^7	$1024 \times 1 \times 512$	35.4	3.26×10^3	33.5	32.4	35.4	0.13	0.13	1.5
10^3	5×10^7	$2048 \times 1 \times 1024$	57.7	8.79×10^3	38.0	36.7	57.3	0.080	0.078	1.7
∞	1×10^5	$128 \times 1 \times 64$	9.8	1.98×10^2	22.3	22.3	9.8	0.60	0.60	4.5
∞	5×10^5	$128 \times 1 \times 64$	16.0	5.37×10^2	26.1	26.1	16.1	0.36	0.36	2.7
∞	1×10^6	$256 \times 1 \times 128$	19.8	2.25×10^2	27.6	27.6	19.8	0.29	0.29	4.3
∞	5×10^6	$512 \times 1 \times 128$	32.6	2.27×10^3	30.8	30.8	32.6	0.17	0.17	3.6
∞	1×10^7	$512 \times 1 \times 256$	40.5	3.52×10^3	31.9	31.9	40.5	0.14	0.14	4.0
∞	5×10^7	$1024 \times 1 \times 256$	60.0	9.51×10^3	33.5	32.6	60.0	0.077	0.075	3.5
∞	1×10^8	$1024 \times 1 \times 512$	74.3	1.49×10^4	33.9	32.9	74.7	0.061	0.059	3.9
∞	5×10^8	$2048 \times 1 \times 512$	124	4.27×10^4	34.8	33.7	124	0.036	0.034	3.2
10^2	1.0×10^5	256^3	9.8	1.98×10^2	22.3	22.3	9.8	0.60	0.60	1.9
10^2	6.5×10^5	256^3	17.3	6.15×10^2	28.6	28.3	17.5	0.36	0.34	1.0
10^2	2.0×10^6	512^3	24.1	1.20×10^3	32.1	32.2	24.1	0.25	0.24	1.4
10^2	5.0×10^6	512^3	31.0	1.96×10^3	39.5	39.1	30.9	0.19	0.19	1.1
10^2	1.0×10^7	1024^3	38.1	2.92×10^3	43.7	43.4	38.2	0.16	0.16	1.7
10^3	6.5×10^4	256^3	8.6	1.53×10^2	21.4	21.4	8.6	0.69	0.68	1.3
10^3	1.0×10^5	256^3	9.8	1.98×10^2	22.3	22.3	9.8	0.60	0.60	1.1
10^3	3.2×10^5	512^3	14.1	3.98×10^2	27.2	27.1	14.1	0.42	0.43	1.5
10^3	2.0×10^6	1024^3	24.3	1.10×10^3	38.7	38.3	24.3	0.26	0.26	1.6
10^3	6.0×10^6	1024^3	34.2	2.13×10^3	43.4	43.7	34.2	0.19	0.19	1.1
∞	7.0×10^4	128^3	8.8	1.59×10^2	21.4	21.6	8.8	0.67	0.68	1.7
∞	3.2×10^5	128^3	14.1	4.14×10^2	25.1	25.1	14.1	0.41	0.42	2.0
∞	6.5×10^5	128^3	17.4	6.36×10^2	26.7	26.7	17.4	0.33	0.34	1.6
∞	3.9×10^6	256^3	30.3	1.95×10^3	30.3	30.4	30.3	0.19	0.19	1.8
∞	6.5×10^6	256^3	36.1	2.70×10^3	33.5	31.8	36.0	0.16	0.16	1.5
∞	9.8×10^6	256^3	41.2	3.34×10^3	35.8	35.6	41.1	0.15	0.15	1.3
∞	1.0×10^8	512^3	87.5	1.38×10^4	45.6	45.3	87.2	0.07	0.07	1.3

advancement, and 2/3 rule for dealiasing. We use the pseudospectral code TARANG [15] for our simulations. More details about the numerical scheme can be found in ref. [12].

We perform direct numerical simulations (DNS) for Prandtl numbers 10^2, 10^3, and ∞ and Rayleigh numbers in the range 10^5 to 5×10^8. The parameters and grid resolutions of all our runs are listed in table 1. Our grid resolution is such that the Batchelor length scale is larger than the mean grid spacing, thus ensuring that our simulations are fully resolved. Quantitatively, $k_{\max}\eta_\theta \geqslant 1$ for all the runs, where $k_{\max}$ is the maximum wavenumber (inverse of the smallest length scale), and $\eta_\theta = (\kappa^3/\epsilon_u)^{1/4}$ is the Batchelor length.

We also perform simulations for $\mathrm{Pr} = 10^2$ in a 2D box of aspect ratio one with no-slip boundary condition on all sides. We use the spectral element code NEK5000 [16]. The Rayleigh number is varied from 10^4 to 5×10^7. We chose a box with 28×28 spectral elements and seventh-order polynomials within each element, and therefore the overall grid resolution is 196^2. For the spectra study, however, we use 15th-order polynomials that yield 420^2 effective grid points in the box.

We compute the energy and entropy spectra and fluxes, Nusselt and Péclet numbers, temperature fluctuations, and dissipation rates using the numerical data of the steady state. These quantities are averaged over 2000 eddy turnover times.

4. Low-wavenumber Fourier modes of 2D and 3D flows

Schmalzl *et al* [2,3] and van der Poel *et al* [4] showed that the flow of 3D RBC quite closely resembles the 2D flow for large Prandtl numbers. The temperature isosurfaces for $\mathrm{Pr} = \infty$ shown in figure 1 illustrates an array of parallel rolls, thus suggesting a quasi-two-dimensional structure for the flow. For 2D RBC, the temperature field exhibited in figure 2 for $\mathrm{Pr} = 10^3, \infty$, and $\mathrm{Ra} = 10^6$ quite closely resembles the rolls of 3D RBC. This similarity is because the most dominant θ modes are common among 2D and 3D RBC (to be discussed below). We also remark that at large Rayleigh numbers, the plumes become somewhat turbulent, as shown in figure 3 for $\mathrm{Ra} = 5 \times 10^7$ and $\mathrm{Pr} = 100, 1000, \infty$.

For comparison between the 2D and 3D RBC, we perform 2D and 3D simulations for $\mathrm{Pr} = \infty$ and $\mathrm{Ra} = 10^7$. The first six most dominant θ modes are $(0, 0, 2n) \approx -1/(2n\pi)$, where $n = 1$ to 6, as

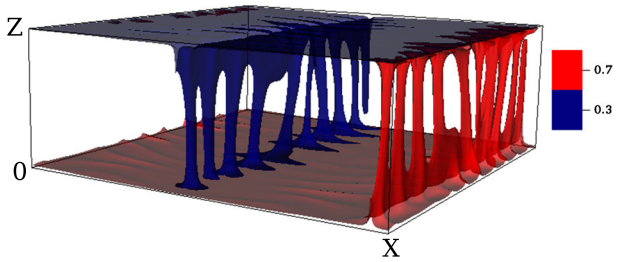

Figure 1. Temperature isosurfaces for $\mathrm{Pr} = \infty$ and $\mathrm{Ra} = 6.6 \times 10^6$ exhibiting sharp plumes and quasi-2D nature of 3D RBC. The red (blue) structures represent hot (cold) fluid going up (down) (figure adapted from Pandey *et al* [13]).

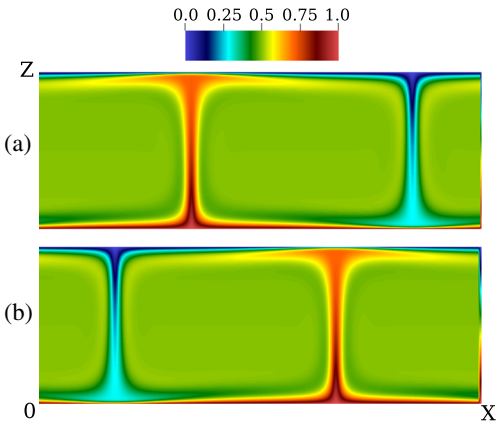

Figure 2. Density plots of the temperature field in a 2D box for $\mathrm{Ra} = 10^6$ and (**a**) $\mathrm{Pr} = 10^3$; (**b**) $\mathrm{Pr} = \infty$. The figures illustrate hot (red) and cold (blue) plumes.

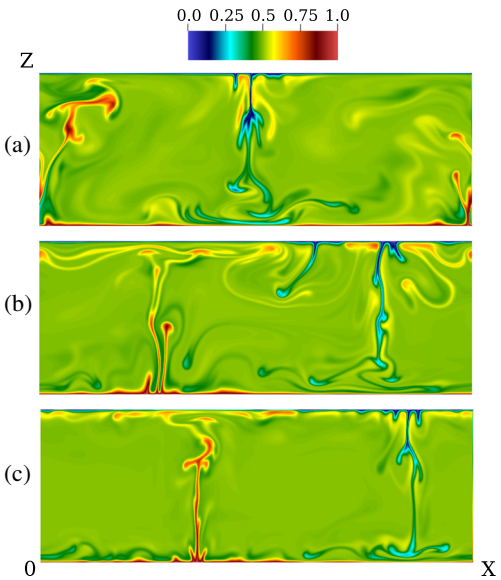

Figure 3. Density plots of the temperature field for $\mathrm{Ra} = 5 \times 10^7$ and (**a**) $\mathrm{Pr} = 10^2$; (**b**) $\mathrm{Pr} = 10^3$; (**c**) $\mathrm{Pr} = \infty$. The structures get sharper with increasing Prandtl numbers [4].

Table 2. Comparison of the ten most dominant entropy Fourier modes in 2D and 3D RBC for $\mathrm{Pr} = \infty$ and $\mathrm{Ra} = 10^7$. Here (n_x, n_y, n_z) are mode indices which are related to a mode $\mathbf{k}$ as $(k_x, k_y, k_z) = (\frac{\pi}{\sqrt{2}} n_x, \frac{\pi}{\sqrt{2}} n_y, \pi n_z)$.

Mode (3D) (n_x, n_y, n_z)	$E_\theta^{\mathrm{mode}}/E_\theta^{\mathrm{3D}}$ (%)	$E_u^{\mathrm{mode}}/E_u^{\mathrm{3D}}$ (%)	Mode (2D) (n_x, n_z)	$E_\theta^{\mathrm{mode}}/E_\theta^{\mathrm{2D}}$ (%)	$E_u^{\mathrm{mode}}/E_u^{\mathrm{2D}}$ (%)
(0,0,2)	30.4	0	(0,2)	30.6	0
(0,0,4)	7.81	0	(0,4)	7.79	0
(0,0,6)	3.56	0	(0,6)	3.54	0
(0,0,8)	2.03	0	(0,8)	2.03	0
(0,0,10)	1.30	0	(0,10)	1.31	0
(0,0,12)	0.87	0	(0,12)	0.90	0
(1,0,1)	0.018	19.6	(1,1)	0.020	20.4
(3,0,1)	0.011	2.05	(3,1)	0.018	3.39
(1,0,3)	0.011	0.046	(1,3)	0.011	0.046
(3,0,3)	0.003	0.039	(3,3)	0.007	0.095

shown by Mishra and Verma [12]; for these modes $\mathbf{u}(\mathbf{k}) = 0$ [see eq. (12)]. In table 2, we list the ten most dominant temperature modes along with their entropy and kinetic energy. According to table 2, the entropy and the kinetic energy of the top ten modes, (k_x, k_z) in 2D and $(k_x, 0, k_z)$ in 3D, are very close. This is the reason for the flow structures of the 3D RBC to be quasi-two-dimensional.

Apart from $\hat{\theta}(0, 0, 2n)$ modes, the next four most dominant 2D modes are $(1, 1), (3, 1), (1, 3)$, and $(3, 3)$. Clearly, $(1, 1)$ is the most dominant mode with a finite kinetic energy, and it corresponds to a pair of rolls shown in figures 1–3. The mode $(1, 1)$ is a part of the most dominant triad interaction $\{(1, 1), (-1, 1), (0, 2)\}$ [12]. The other modes $(3, 1), (1, 3)$ arise due to nonlinear interaction with the $(2, 2)$ mode, which is relatively weak but quite important [17].

We also compute the total energy of the three components of the velocity field in 3D and the two components in 2D. We observe that in 3D, $E_x/E_u = 0.55$, $E_y/E_u = 0.02$, and $E_z/E_u = 0.43$, clearly demonstrating the quasi-2D nature of the flow. Here, $E_x = \langle u_x^2 \rangle/2$, $E_y = \langle u_y^2 \rangle/2$, $E_z = \langle u_z^2 \rangle/2$, $E_u = E_x + E_y + E_z$, and $\langle \cdot \rangle$ represents the time-averaged value in the steady state. In 2D, the ratios are $E_x/E_u = 0.58$ and $E_z/E_u = 0.42$, which are quite close to the corresponding ratios for the 3D RBC.

We also performed similar analysis for $\mathrm{Pr} = 100$ and 1000 for 2D and 3D, whose behaviour is similar to that for $\mathrm{Pr} = \infty$ described above.

Schmalzl *et al* [2,3] decomposed the 3D velocity field into toroidal and poloidal components, and showed that the toroidal component disappears in the limit of infinite Prandtl number, consistent with the analytical results of Vitanov [18]. Schmalzl *et al* [2] argued that the vertical component of the vorticity disappears in the $\mathrm{Pr} = \infty$ limit, leading to vanishing of the toroidal component of the velocity, and hence the two-dimensionalization of the $\mathrm{Pr} = \infty$ RBC. Our results are consistent with those of Schmalzl *et al* [2,3] and Vitanov [18].

5. Energy spectra and fluxes

In this section, we compute the spectra and fluxes of energy and entropy for 2D and 3D RBC for large and infinite Prandtl numbers and compare them. We show that these quantities are very close to each other for 2D and 3D RBC because the dominant Fourier modes for them are very close to each other.

The one-dimensional kinetic energy and entropy spectra are defined as

$$E_u(k) = \sum_{k \le |\mathbf{k}'| < k+1} \frac{|\hat{\mathbf{u}}(\mathbf{k}')|^2}{2}, \tag{15}$$

$$E_\theta(k) = \sum_{k \le |\mathbf{k}'| < k+1} \frac{|\hat{\theta}(\mathbf{k}')|^2}{2}. \tag{16}$$

The flow is anisotropic in 2D RBC, e.g., $E_x/E_z = 1.37$, but the degree of anisotropy is rather small. Hence, the aforementioned one-dimensional spectra give a good description of the flow properties.

The nonlinear interactions induce kinetic energy and entropy transfers from larger length scales to smaller length scales that results in kinetic energy and entropy

fluxes. Note that for $\mathrm{Pr} = \infty$, the nonlinear interaction among the velocity modes is absent, and hence the kinetic energy flux is zero for this case. The kinetic energy and entropy fluxes coming out of a wavenumber sphere of radius k_0 are given by [12,19]

$$\Pi_u(k_0) = \sum_{k\geq k_0}\sum_{p<k_0} \delta_{\mathbf{k},\mathbf{p}+\mathbf{q}}\Im \times([\mathbf{k}\cdot\hat{\mathbf{u}}(\mathbf{q})][\hat{\mathbf{u}}^*(\mathbf{k})\cdot\hat{\mathbf{u}}(\mathbf{p})]), \quad (17)$$

$$\Pi_\theta(k_0) = \sum_{k\geq k_0}\sum_{p<k_0} \delta_{\mathbf{k},\mathbf{p}+\mathbf{q}}\Im \times([\mathbf{k}\cdot\hat{\mathbf{u}}(\mathbf{q})][\hat{\theta}^*(\mathbf{k})\cdot\hat{\theta}(\mathbf{p})]), \quad (18)$$

where $\Im$ stands for the imaginary part of the argument and $\mathbf{k}$, $\mathbf{p}$ and $\mathbf{q}$ are the wavenumbers of a triad with $\mathbf{k} = \mathbf{p} + \mathbf{q}$.

For 3D RBC with $\mathrm{Pr} = \infty$, Pandey *et al* [13] derived the kinetic energy and entropy spectra as

$$E_u(k) = (a_2^2 a_3)^{2/3} d\left(\frac{\kappa}{d}\right)^2 \mathrm{Ra}^{(2/3)(3-2\delta-\zeta)}(kd)^{-13/3}, \quad (19)$$

$$E_\theta(k) = (a_2^2 a_3)^{2/3} d\Delta^2 \mathrm{Ra}^{(2/3)(\delta-\zeta)}(kd)^{-1/3}, \quad (20)$$

where a_2, a_3, ζ and δ are defined using $\theta_{\mathrm{rms}} = a_2\Delta$, $\mathrm{Pe} = a_3\mathrm{Ra}^{1-\zeta}$, and $\theta_{\mathrm{res}} \sim \mathrm{Ra}^{\delta}$. θ_{res} is the temperature fluctuation without $\hat{\theta}(0, 0, 2n)$ modes [13]. They also argued that the kinetic energy flux $\Pi_u(k) \to 0$, but $\Pi_\theta(k) \approx$ const. in the inertial range for $\mathrm{Pr} = \infty$ RBC. They showed that the above formulae also describe the energy spectra for very large Prandtl numbers, i.e., for $\mathrm{Pr} > 100$.

The arguments of Pandey *et al* [13] are independent of dimensionality, and hence we expect the above expressions to hold in 2D as well for large and infinite Prandtl numbers. In fact, the similarities must be very close because of the identical dominant Fourier modes in 2D and 3D RBC (see §4). To verify the above conjecture, we compute the energy and entropy spectra, as well as their fluxes.

In figure 4, we plot the normalized kinetic spectrum $E_u(k)k^{13/3}$ for $\mathrm{Pr} = 100, \mathrm{Ra} = 10^7$ and $\mathrm{Pr} = \infty, \mathrm{Ra} = 10^8$ for both 2D and 3D RBC. The figure illustrates that the energy spectrum for 2D and 3D are quite close. Hence, our conjecture that 2D and 3D RBC exhibit similar kinetic energy spectrum is verified. Figure 5 exhibits the kinetic spectrum for an RBC simulation in a unit box with no-slip boundary condition for $\mathrm{Pr} = 100$ and $\mathrm{Ra} = 10^7$. The figure demonstrates that $E_u(k) \sim k^{-13/3}$, similar to that of free-slip boundary condition.

The kinetic energy flux Π_u for $\mathrm{Pr} = \infty$ is zero due to the absence of nonlinearity. However, Π_u is expected

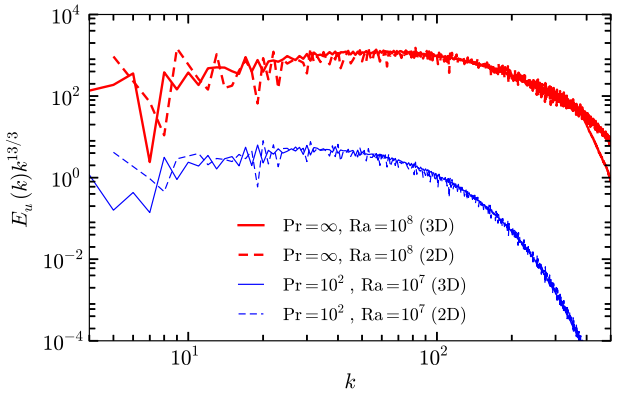

Figure 4. The normalized kinetic energy spectrum $E_u(k)k^{13/3}$ as a function of wavenumber. Curves for 2D and 3D collapse on each other and are nearly constant in the inertial range, and hence $E_u(k) \sim k^{-13/3}$.

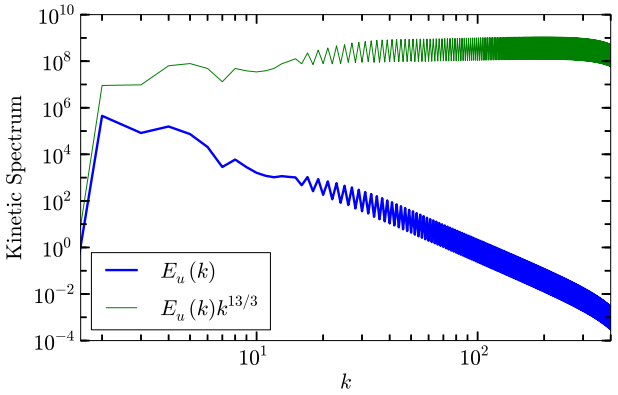

Figure 5. The kinetic energy spectrum $E_u(k)$ for $\mathrm{Pr} = 10^2$ and $\mathrm{Ra} = 10^7$ in a 2D unit box with no-slip boundary condition. The normalized spectrum is nearly constant in the inertial range, and hence $E_u(k) \sim k^{-13/3}$ (figure adapted from Pandey *et al* [13]).

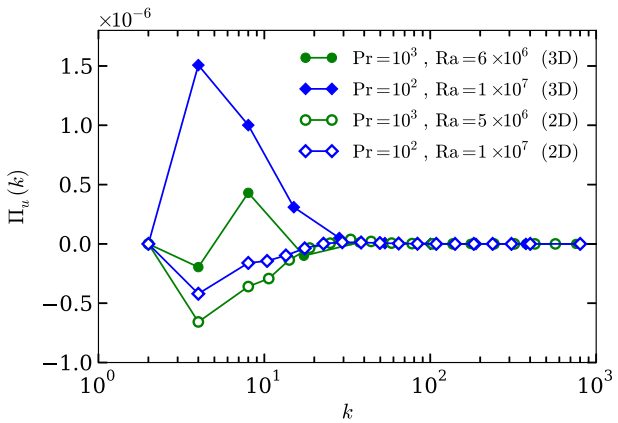

Figure 6. Plot of the kinetic energy flux $\Pi_u(k)$ vs. k. The fluxes for $\mathrm{Pr} = 10^2$ have been multiplied by a factor of 10^{-2} to fit properly in this figure. In 2D, $\Pi_u(k) < 0$, reminiscence of 2D fluid turbulence.

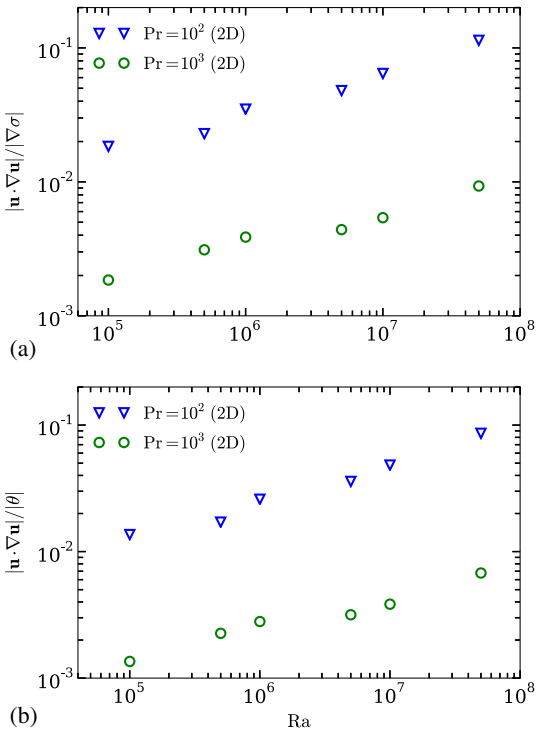

Figure 7. Plots of the ratios between (**a**) nonlinear and pressure gradient terms and (**b**) nonlinear and buoyancy terms of eq. (1). The nonlinearity is weak compared to pressure gradient and buoyancy.

to be small ($\ll 1$ in our normalized units) for large Pr. In figure 6, we plot the kinetic energy flux $\Pi_u(k)$ for $\mathrm{Pr} = 10^2$ and 10^3 for 2D and 3D RBC. As expected, Π_u values are small for all the four cases. Interestingly, the kinetic energy flux for 2D RBC is negative at small wavenumbers, which is reminiscent of 2D fluid turbulence [9,20]. The KE flux for 3D RBC is positive almost everywhere. Thus, the KE fluxes for 2D and 3D RBC are somewhat different, but they play an insignificant role in the large and infinite Prandtl number RBC. Hence, we can claim that a common feature for the large Pr 2D and 3D RBC is that $\Pi_u \to 0$.

The reason for the smallness of kinetic energy flux for the large and infinite Pr RBC is that the nonlinear term is much weaker than the pressure gradient and the buoyancy terms of eq. (1). In figure 7, we plot $|\mathbf{u}\cdot\nabla\mathbf{u}|/|\nabla\sigma|$ and $|\mathbf{u}\cdot\nabla\mathbf{u}|/|\theta|$ as a function of Ra. The aforementioned ratios lie between 0.001 and 0.1, and they become smaller as Pr increases. These results show that the nonlinear term is weak for large and infinite Pr RBC. Note that $|\nabla\sigma| \approx |\theta|$, consistent with eq. (13).

In figure 8, we plot the entropy spectrum for $\mathrm{Pr} = 100, \mathrm{Ra} = 10^7$ and $\mathrm{Pr} = \infty, \mathrm{Ra} = 10^8$ for 2D and 3D RBC. Clearly, the entropy spectrum for the 2D and 3D RBC also show very similar behaviour. Note that

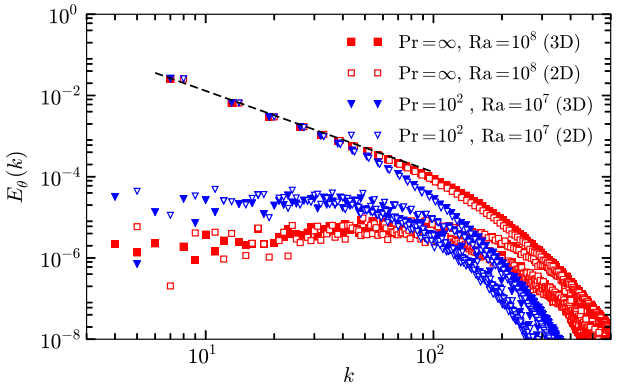

Figure 8. Entropy spectrum $E_\theta(k)$ vs. k. $E_\theta(k)$ exhibits a dual branch with a dominant upper branch with $E_\theta(k) \sim k^{-2}$. The lower branch is almost flat in the inertial range.

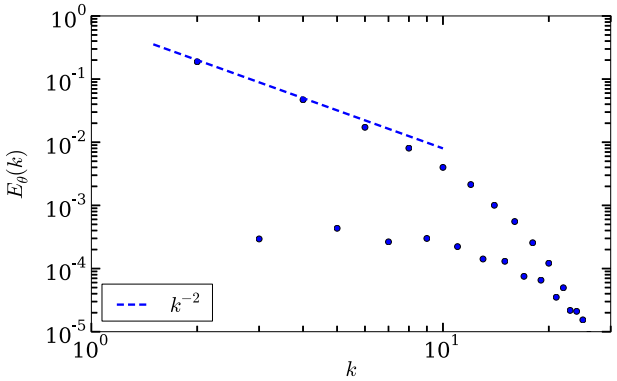

Figure 9. Entropy spectrum $E_\theta(k)$ for $\mathrm{Pr} = 10^2$ and $\mathrm{Ra} = 10^7$ with no-slip boundary condition in a 2D box. Its behaviour is very similar to that for the free-slip boundary condition (figure adapted from Pandey *et al* [13]).

the entropy spectrum exhibits a dual spectrum, with the top curve ($E(k) \sim k^{-2}$) representing the $\hat{\theta}(0, 0, 2n)$ modes, whose values are close to $-1/(2n\pi)$ (see §4 and Mishra and Verma [12]). The lower curve in the spectrum, corresponding to modes other than $\hat{\theta}(0, 0, 2n)$, is somewhat flat. We also observe similar entropy spectrum for no-slip boundary condition, which is shown in figure 9 for $\mathrm{Pr} = 100$ and $\mathrm{Ra} = 10^7$.

We compute the entropy flux defined in eq. (18) [12] for $\mathrm{Pr} = 100$, $\mathrm{Ra} = 10^7$ and $\mathrm{Pr} = \infty$, $\mathrm{Ra} = 10^8$ for both 2D and 3D RBC. In figure 10, we plot the entropy flux $\Pi_\theta(k)$ for the above four cases. Clearly, the behaviour of 2D and 3D RBC are very similar, with a constant entropy flux in the inertial range.

In the next section, we shall compute large-scale quantities for 2D and 3D RBC with large and infinite Prandtl numbers.

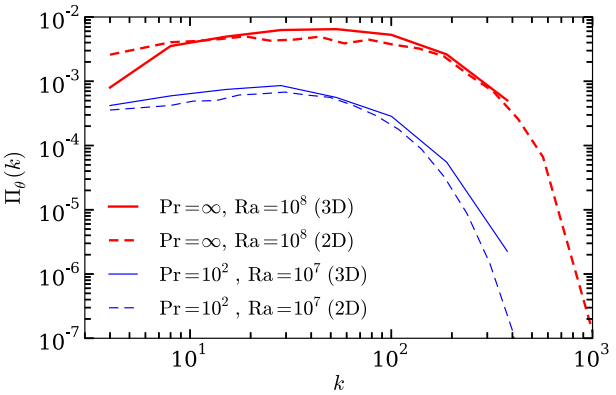

Figure 10. Plot of the entropy flux $\Pi_\theta(k)$ vs. k. The fluxes are nearly constant in the inertial range, and are similar for the 2D and 3D RBC.

6. Scaling of large-scale quantities

6.1 *Nusselt and Péclet numbers*

Schmalzl *et al* [2,3] and van der Poel *et al* [4] showed that the Nusselt and Péclet numbers for 2D and 3D RBC exhibit similar scaling. For validation of our data, we also compute the Nusselt number Nu and Péclet number Pe, as well as $\theta_{\rm rms}$ using our data sets.

In figure 11, we plot the Nusselt number, Péclet number and normalized root mean square temperature fluctuations for Pr $=$ 100, 1000, ∞ and Ra ranging from 10^4 to 5×10^8 for both 2D and 3D RBC. We also plot Nu and Pe for Pr $=$ 100 with no-slip boundary condition (shown by orange triangles). The figures show that the 2D and 3D RBC have similar Nusselt and Péclet number scaling, in particular Nu $\sim$ Ra$^{0.3}$ and Pe $\sim$ Ra$^{0.6}$, with a weak variation of the exponents with Pr and Ra. However, the Nu and Pe prefactors for the no-slip data are lower than those for free-slip runs, which is due to lower frictional force for the free-slip boundary condition. These results are consistent with those of Schmalzl *et al* [2,3], van der Poel *et al* [4], Silano *et al* [14], and Pandey *et al* [13].

We observe that $\theta_{\rm rms}/\Delta$ is a constant. The details of scaling and error bars are discussed in Pandey *et al* [13]. These similarities are primarily due to the quasi-2D nature of the 3D RBC.

6.2 *Dissipation rates*

In this subsection, we shall discuss the scaling of normalized viscous and thermal dissipation rates for large Prandtl numbers. Shraiman and Siggia [21] derived the following exact relations between dissipation rates, Pr, Ra, and Nu:

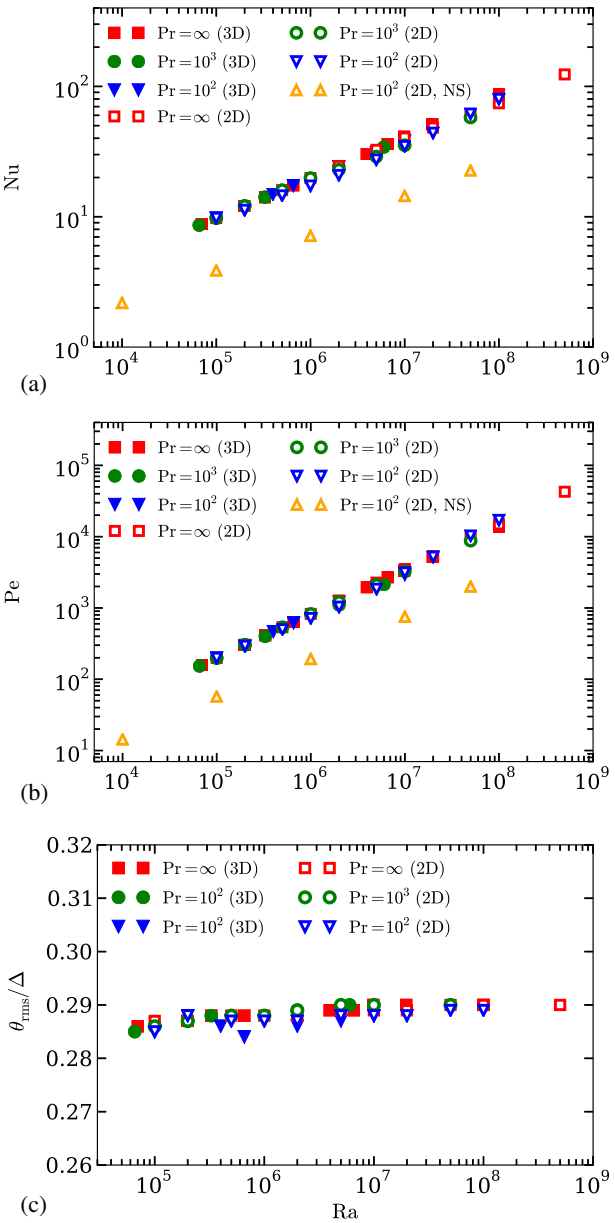

Figure 11. Plots of (**a**) Nusselt number Nu; (**b**) Péclet number Pe; (**c**) normalized root mean square temperature fluctuations $\theta_{\rm rms}/\Delta$ as a function of Rayleigh number. The 2D and 3D RBC exhibit similar scaling for large-scale quantities, except for the no-slip data for Pr $=$ 100 (orange triangles), for which the prefactors are lower.

$$\epsilon_u = \nu\langle|\nabla \times \mathbf{u}|^2\rangle = \frac{\nu^3}{d^4}\frac{(\mathrm{Nu}-1)\mathrm{Ra}}{\mathrm{Pr}^2}, \tag{21}$$

$$\epsilon_T = \kappa\langle|\nabla T|^2\rangle = \kappa\frac{\Delta^2}{d^2}\mathrm{Nu}, \tag{22}$$

where ϵ_u and ϵ_T are the volume-averaged viscous and thermal dissipation rates, respectively. For large and

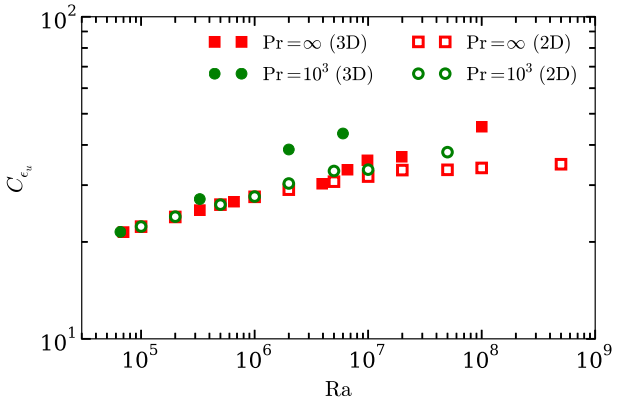

Figure 12. Normalized viscous dissipation rate C_{ϵ_u} as a function of Ra. The values of C_{ϵ_u} are lower in 2D compared to the values in 3D RBC.

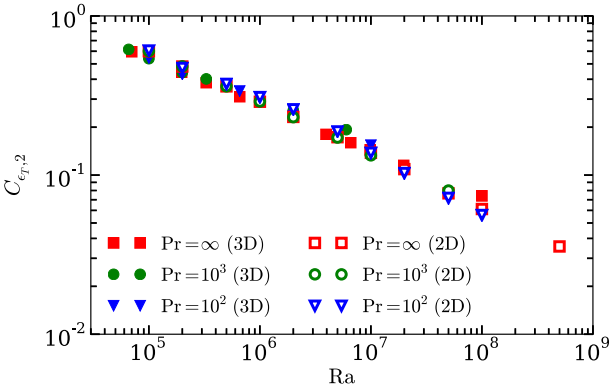

Figure 13. Normalized thermal dissipation rate $C_{\epsilon_T,2}$ as a function of Rayleigh number. We observe $C_{\epsilon_T,2} \sim \mathrm{Ra}^{-0.32}$ in 2D, which is similar to the scaling for $\mathrm{Pr} = \infty$ in 3D.

infinite Prandtl numbers, which correspond to the viscous dominated regime, an appropriate formula for the normalized viscous dissipation rate is [13]

$$C_{\epsilon_u} = \frac{\epsilon_u}{\nu U_L^2/d^2} = \frac{(\mathrm{Nu}-1)\mathrm{Ra}}{\mathrm{Pe}^2}. \tag{23}$$

The corresponding formulas for the normalized thermal dissipation rate are

$$C_{\epsilon_T,1} = \frac{\epsilon_T}{\kappa\Delta^2/d^2} = \mathrm{Nu}, \tag{24}$$

$$C_{\epsilon_T,2} = \frac{\epsilon_T}{U_L\theta_L^2/d} = \frac{\mathrm{Nu}}{\mathrm{Pe}}\left(\frac{\Delta}{\theta_L}\right)^2. \tag{25}$$

See Pandey *et al* [13] for a detailed discussion on the dissipation rates for large Prandtl number convection.

Using the scaling of Nu and Pe, we find that for $\mathrm{Pr} = \infty$, C_{ϵ_u} is an approximate constant independent of Ra [13]. In figure 12, we plot C_{ϵ_u} for $\mathrm{Pr} = 10^3$ and ∞, according to which C_{ϵ_u} is nearly a constant with a significant scatter of data. As evident from the figure, the normalized viscous dissipation rate for the 2D RBC is a bit lower than the corresponding data for the 3D RBC, which is due to the inverse cascade of energy in 2D RBC that suppresses Π_u (see figure 6).

In table 1, we list the normalized thermal dissipation rate $C_{\epsilon_T,1}$ and the Nusselt number, and they are observed to be quite close to each other, consistent with eq. (24). In the table, we also list the computed dissipation rate $C_{\epsilon_T,2}^{\mathrm{comp.}} = \epsilon_T/(U_L\theta_L^2/d)$ and the estimated dissipation rate $C_{\epsilon_T,2}^{\mathrm{est.}} = (\mathrm{Nu}/\mathrm{Pe})(\Delta/\theta_L)^2$, where $U_L = \sqrt{2E_u}$ and $\theta_L = \sqrt{2E_\theta}$. These quantities are close to each other, consistent with eq. (25).

Figure 13 exhibits $C_{\epsilon_T,2}$ as a function of Ra. The figure shows that the scaling of $C_{\epsilon_T,2}$ in 2D is similar to that for 3D RBC. A detailed analysis indicates that for 2D RBC, $C_{\epsilon_T,2} = (22 \pm 9)\mathrm{Ra}^{-0.31\pm0.03}$, $(24 \pm 1.7)\mathrm{Ra}^{-0.32\pm0.01}$, and $(24 \pm 2.1)\mathrm{Ra}^{-0.32\pm0.01}$ for $\mathrm{Pr} = 10^2$, 10^3, and ∞, respectively. For 3D RBC, Pandey *et al* [13] reported $C_{\epsilon_T,2} = (17 \pm 5.1)\mathrm{Ra}^{-0.29\pm0.02}$, $(16 \pm 4.1)\mathrm{Ra}^{-0.28\pm0.02}$, and $(22 \pm 2.2)\mathrm{Ra}^{-0.31\pm0.01}$ for $\mathrm{Pr} = 10^2$, 10^3, and ∞, respectively. The scaling of $C_{\epsilon_T,2}$ for 2D and 3D RBC are similar.

These computations show that the behaviour of viscous and thermal dissipation rates for 2D and 3D RBC are quite similar.

7. Discussions and conclusions

We performed numerical simulations of 2D and 3D RBC for $\mathrm{Pr} = 100, 1000, \infty$, and Ra in the range of 10^5 to 5×10^8. We showed that the dominant Fourier modes of the 2D and 3D flows are very close to each other, which is the reason for the similarities between the Nusselt and Péclet numbers in 2D and 3D RBC, as reported by Schmalzl *et al* [2,3] and van der Poel *et al* [4]. The flow in 3D RBC is quasi-two-dimensional because of the strong suppression of the velocity in one of the horizontal directions. These results are consistent with the results of Schmalzl *et al* [2,3] and Vitanov [18], according to which the toroidal component of the velocity field in 3D RBC vanishes for $\mathrm{Pr} = \infty$.

We compute the spectra and fluxes of the kinetic energy and entropy for the 2D RBC and show them to be very similar to those for the 3D RBC. In particular, we observe that the kinetic energy spectrum $E_u(k) \sim k^{-13/3}$, while the entropy spectrum exhibits a dual branch, with a dominant k^{-2} branch corresponding

to the $\hat{\theta}(0, 0, 2n)$ Fourier modes. The other entropy branch is somewhat flat. The similarities between the spectra and fluxes of 2D and 3D RBC are due to the quasi-2D nature of 3D RBC.

We compute global quantities such as the Nusselt and Péclet numbers, $\theta_{\rm rms}$, the kinetic energy and thermal dissipation rates. All these quantities exhibit similar behaviour in 2D and 3D RBC, which is consistent with the results of Schmalzl *et al* [2,3] and van der Poel *et al* [4].

Our results are essentially numerical. It will be useful to construct low-dimensional models of $\mathrm{Pr} = \infty$ convection, and study how the velocity in one of the perpendicular direction gets suppressed. This work is under progress.

Acknowledgements

The numerical simulations were performed at HPC and Newton clusters of IIT Kanpur, and at Param Yuva cluster of CDAC Pune. This work was supported by a research grant SERB/F/3279/2013-14 from Science and Engineering Research Board, India. The authors thank Supriyo Paul for useful comments and sharing his earlier results on 2D RBC. The authors also thank A Kumar for providing help in flow visualization.

References

[1] G Ahlers, S Grossmann and D Lohse, *Rev. Mod. Phys.* **81**, 503 (2009)
[2] J Schmalzl, M Breuer and U Hansen, *Geophys. Astrophys. Fluid Dyn.* **96**, 381 (2002)
[3] J Schmalzl, M Breuer and U Hansen, *Europhys. Lett.* **67**, 390 (2004)
[4] E P van der Poel, R J A M Stevens and D Lohse, *J. Fluid Mech.* **736**, 177 (2013)
[5] D Lohseand and K Q Xia, *Annu. Rev. Fluid Mech.* **42**, 335 (2010)
[6] S Grossmann and D Lohse, *Phys. Rev. A* **46**, 903 (1992)
[7] V S L'vov, *Phys. Rev. Lett.* **67**, 687 (1991)
[8] V S L'vov and G Falkovich, *Physica D* **57**, 85 (1992)
[9] S Toh and E Suzuki, *Phys. Rev. Lett.* **73**, 1501 (1994)
[10] A P Vincent and D A Yuen, *Phys. Rev. E* **60**, 2957 (1999)
[11] A P Vincent and D A Yuen, *Phys. Rev. E* **61**, 5241 (2000)
[12] P K Mishra and M K Verma, *Phys. Rev. E* **81**, 056316 (2010)
[13] A Pandey, M K Verma and P K Mishra, *Phys. Rev. E* **89**, 023006 (2014)
[14] G Silano, K R Sreenivasan and R Verzicco, *J. Fluid Mech.* **662**, 409 (2010)
[15] M K Verma, A G Chatterjee, K S Reddy, R K Yadav, S Paul, M Chandra and R Samtaney, *Pramana – J. Phys.* **81**, 617 (2013)
[16] P F Fischer, *J. Comp. Phys.* **133(1)**, 84 (1997)
[17] M Chandra and M K Verma, *Phys. Rev. Lett.* **110**, 114503 (2013)
[18] N K Vitanov, *Phys. Lett. A* **248**, 338 (1998)
[19] M K Verma, *Phys. Rep.* **401**, 229 (2004)
[20] G Boffetta and R E Ecke, *Annu. Rev. Fluid Mech.* **44**, 427 (2012)
[21] B I Shraiman and E D Siggia, *Phys. Rev. A* **42**, 3650 (1990)